FISEVIER

Contents lists available at ScienceDirect

## Journal of Manufacturing Processes

journal homepage: www.elsevier.com/locate/manpro





# Laser directed energy deposition additive manufacturing using friction stir channelling extruded wire

Yajie Chu a,b, Xingjian Zhao ,Wanting Sun ,Sam Holdsworth ,Dikai Guan ,Yuze Huang ,Yuze Huang ,

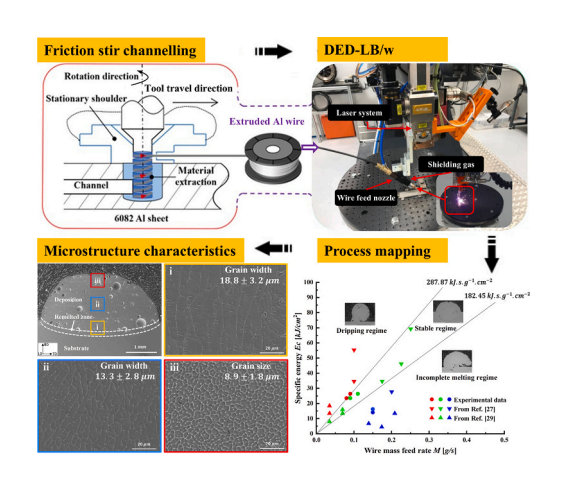
- a Department of Engineering, Lancaster University, Lancaster, LA1 4YW, UK
- <sup>b</sup> School of Materials Science and Engineering, Nanjing Institute of Technology, Nanjing, Jiangsu, 211167, China
- <sup>c</sup> Department of Mechanical Engineering, School of Engineering, University of Southampton, Southampton, SO17 1BJ, UK
- <sup>d</sup> TWI Ltd., Cambridge, CB21 6AL, UK
- e Laser Processing Research Laboratory, School of Engineering, The University of Manchester, Manchester M13 9PL, UK

#### HIGHLIGHTS

#### Directed energy deposition employs novel friction stir channelling extruded wire.

- Process mapping is built to demarcate melting regimes based on processing parameters.
- Fine grain size (9–20 $\mu$ m) is achieved in the additive builds though with porosity.
- Gas entrapment and oxides are identified as the primary sources of porosity.

#### G R A P H I C A L A B S T R A C T



## ARTICLE INFO

Keywords:
Additive manufacturing
Stationary shoulder friction stir channelling
(SS-FSC)
Directed energy deposition with a laser beam
and wire feedstock (DED-LB/w)
Process mapping
Porosity defect
Microstructure

## ABSTRACT

This paper investigates a new 'forged' wire additive manufacturing processing, in which the metal wire is produced as a by-product from stationary shoulder friction stir channelling (SS-FSC) under the severe plastic deformation mechanism (known as CoreFlow®), and then used as the feedstock in directed energy deposition with a laser beam and wire feedstock (DED-LB/w) additive manufacturing. For the first time, the 'by-products' produced in the SS-FSC process, which are 'forged' 6082 aluminium alloy wire, were tested with built-tracks using DED-LB/w. Process mapping was built to demarcate the melting states, including the stable, dripping, and incomplete melting regimes, over a wide range of laser energy densities (92 to 303  $kJ \cdot s \cdot g^{-1} \cdot cm^{-2}$ ). Metallurgy tests were also conducted to reveal the evolution of the microstructure and defect formation of the deposited tracks. It was found that: (i) Stable deposition with a grain size of  $9 - 20 \, \mu m$  can be achieved with optimised processing parameters, i.e., energy density  $243 \, kJ \cdot s \cdot g^{-1} \cdot cm^{-2}$  with a laser power  $3.8 \, kW$ , a scanning speed  $0.8 \, cm \cdot s^{-1}$  and a wire feed rate  $2.0 \, cm \cdot s^{-1}$ ; (ii) The substructure morphology is gradually transitioned from

E-mail address: y.huang67@lancaster.ac.uk (Y. Huang).

https://doi.org/10.1016/j.jmapro.2025.09.060

<sup>\*</sup> Corresponding author.

columnar at the track bottom to cellular  $(8.9\pm1.8~\mu m)$  at the top, driven by an increased cooling rate; and (iii) The built track porosity is mainly composed of gas pores that are small (equivalent diameter of  $20-50~\mu m$ ) and spherical, primarily resulting from the ambient gas, the SS-FSC extruded wire oxides and contaminations. The study supports resource-efficient, low-carbon manufacturing via reuse of by-products, in alignment with the Net Zero Strategy.

#### 1. Introduction

Directed energy deposition with a laser beam and wire feedstock (DED-LB/w) is an additive manufacturing process where the metal wires are melted by the laser source, creating a localised melt pool and thus achieving the material deposition under a layer-by-layer pattern [1,2]. DED-LB/w excels in precision, material efficiency, and complex part fabrication [3], with precise heat control that minimises distortion and thus enhances properties [4,5]. It is widely applied in aerospace, automotive, and energy industries [6], specialising in large-scale, complex, and lightweight part production for supporting fuel efficiency and sustainability [7,8]. In general, conventional wire production methods, characterised by energy-intensive and resource-consuming processes, increase the overall cost of wire-based additive manufacturing [9]. For instance, producing one ton of Al wire is approximately \$3000 to \$5000. This cost structure ultimately diminishes the sustainability of wire-based directed energy deposition systems [10,11]. Additionally, the traditional process of producing Al alloy wires generates significant amounts of carbon dioxide and wastewater [12,13]. Therefore, it is vital to develop a more economical, recyclable wire feedstock production approach for achieving the NetZero strategy in modern green manufacturing industries [14].

Stationary shoulder friction stir channelling (SS-FSC) [15], an innovative severe plastic deformation (SPD) technology that produces metal alloy wires during the friction stir channelling (FSC) process, has the potential to provide a sustainable wire production solution [16]. During the SS-FSC process, the wire is extruded as a by-product directly from bulk plates during the manufacturing of subsurface channels in the SPD process, i.e. cooling channels for circuits, and battery trays in electric vehicles [9]. SS-FSC technology might offer a better sustainable alternative to conventional wire production approaches that reduce production costs and energy consumption. The utilisation of SS-FSC extruded wire further enhances resource-efficient manufacturing, primarily by enabling the direct repurposing of by-product materials generated during the SS-FSC process, consequently minimising materials waste and raw material demand. This approach aligns with the principles of industrial symbiosis by converting waste streams into valuable input for additive manufacturing, contributing to closed-loop material cycles [10]. Unlike conventional wire production involving energy-intensive processes such as extrusion and multi-stage drawing [11], the advanced SS-FSC offers a potential low-cost and low-energy alternative by eliminating post-processing steps, and thereby both the energy consumption and manufacturing costs are considerably reduced. The development of alternative feedstock sources such as SS-FSC extruded wire supports the broader transition toward sustainable additive manufacturing by reducing dependency on conventional material supply chains.

The SS-FSC process also aligns well with DED-LB/w for achieving green manufacturing and sustainability goals by lowering costs and increasing materials usage [12]. Recently, SS-FSC technology has been successfully employed to produce several light alloy wires, including 6082 aluminium alloy wire that shows excellent mechanical performance with an elongation of 19.3 % and a yield strength of 182 *MPa* [13,14], and AZ31B magnesium alloy wire with an elongation of 22.3 % and a yield strength of 134 *MPa* [15]. Despite its significant potential, this technology may remain insufficiently mature for direct adoption in industrial applications. It faces several challenges, including inconsistent surface quality, surface oxidation, and inhomogeneous composition

of feedstock wire. These issues can affect melt pool stability, deposition quality, and the overall consistency of the deposited tracks. Although there is growing interest in DED-LB/w, the studies on the fundamental process physics when using non-conventional wire feedstock remains limited. The DED-LB/w process involves complex laser—wire—substrate interactions [16], melt pool dynamics, heat transfer [17], and defect evolution (e.g., porosity and incomplete fusion) [18], which are highly dependent on the metallurgical properties of the feedstock. In particular, the behaviour of by-product Al wire extruded via the SS-FSC process under DED-LB/w conditions remains largely unexplored.

Despite extensive research on DED-LB/w, to the best of the authors' knowledge, no investigation has been conducted on the use of SS-FSC extruded wire in the additive manufacturing process, leaving its feasibility for additive manufacturing unverified. This study seeks to bridge this gap by assessing the feasibility of applying the aluminium alloy wire extruded via the SS-FSC process to the laser-wire additive manufacturing process. To achieve this goal, multiple DED-LB/w deposition experiments are conducted using the SS-FSC extruded 6082 aluminium wires under a large range of energy densities. These experiments address the wire processing mapping and reveal the microstructure evolution and building defects. It is found that the stable deposition can be achieved with a grain size of  $9-20 \mu m$  although gas porosity can be induced in the build tracks. The adoption of the SS-FSC extruded 6082 aluminium wires in DED-LB demonstrates their potential to enhance energy efficiency, reduce waste, and support a circular economy through material reuse. This study introduces a new method for industrial by-products in additive manufacturing (AM) and proposes a processability evaluation framework for non-conventional wire feedstock. This framework includes the established comprehensive process map, the microstructure evolution of deposited tracks, and the formation mechanisms and primary sources of porosity defects. It is anticipated that the study can provide the groundwork for sustainable material sourcing and performance optimisation in DED-LB/w processes.

#### 2. Materials and experimental procedures

In this study, 6082 aluminium wire (1.6 mm in Dia.) manufactured by the stationary shoulder friction stir channelling (SS-FSC) process at The Welding Institute (TWI, Cambridge, United Kingdom), was deposited on the sandblasted 6082 aluminium substrate (25 mm  $\times$  100 mm  $\times$ 6 mm) using a house-developed directed energy deposition with a laser beam and wire feedstock (DED-LB/w) additive manufacturing system, as shown in Fig. 1. The SS-FSC extrusion process induces SPD and intense stirring within a confined channel, thereby facilitating material extrusion in the form of a wire. During this operation, the stationary shoulder confines the viscoplastic material's nugget, thus limiting the material flow extracted by the probe. Meanwhile, when combined with the appropriate rotation direction, the probe's specific geometrical features facilitate the partial transfer of the nugget material into the shoulder. As the tool assembly traverses a pre-defined path, this material extraction process results in the formation of two distinct features: (i) an extruded alloy wire, designated as SS-FSC wire, and (ii) a closed subsurface channel within the workpiece [19,20]. This DED-LB/w setup includes a continuous IPG photonics fibre laser (wavelength of 1.07  $\mu m$ , maximum power of 4 kW), an ABB robot and a wire feeder (MFS-V3, Abicor Binzel, United Kingdom). The laser-offset distance was set as 20 mm to enlarge the focus spot size, ensuring it matched the wire

diameter. The wire was fed through a lateral nozzle with an inclined  $40^\circ$  angle to the substrate to improve the quality of deposition. Shielding gas with argon was adopted to prevent oxidation during the DED-LB/w deposition. Table 1 shows the chemical composition of the SS-FSC extruded 6082 aluminium wire. Table 2 lists the major experimental processing parameters. The DED-LB/w parameters were selected based on manufacturer guidelines, preliminary trials, and relevant literature [21,22], and then were systematically optimised to achieve high deposition quality with minimal defects. In this study, all calculations for specific energy density were based on the laser power setting. The reported laser power values of 3.6 kW and 3.8 kW were based on readings from the IPG LaserNet interface. However, it should be noted that these values were not independently calibrated.

The built tracks were cross-sectioned, hot mounted, polished and etched by Weck's reagent. Subsequently, the track width, height, remelted area, and wetting angle were measured using a laser microscope (OLYMPUS LEXT OLS 5000). The microhardness of the track was tested using a Vickers hardness tester (MHV2000) with a 500 g load and a dwell time of 15 s. For microstructure observations, samples were

**Table 1**Chemical composition of the 6082 aluminium wire manufactured by stationary shoulder friction stir channelling (in *wt*%).

Element	Mg	Si	Mn	Fe	Cr	Cu	Zn	Al
Content	0.93	0.89	0.58	0.3	0.06	0.04	0.04	Bal.

**Table 2**Processing parameters for the additive manufacturing of the SS-FSC extruded 6082 aluminium wire using laser-wire directed energy deposition.

Parameters	Values
Laser power [W]	3600, 3800
Laser spot size [mm]	1.8
Scan speed [mm·s <sup>-1</sup> ]	8, 9, 10, 13, 15, 18
Wire feed rate $[mm \cdot s^{-1}]$	15, 16, 17, 20,25, 28, 35
Track length [mm]	50
Shielding gas rate $[L \cdot min^{-1}]$	10

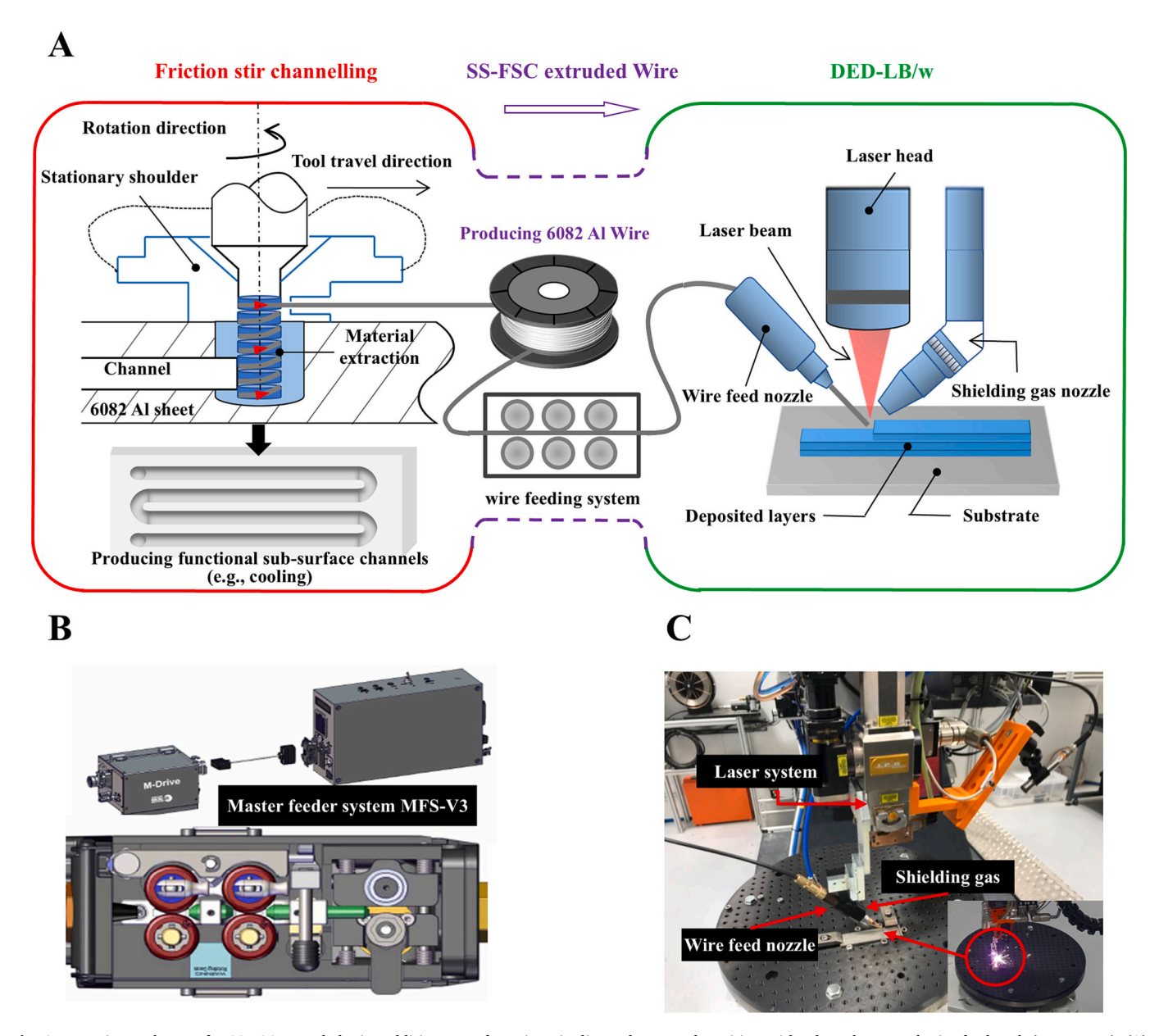


Fig. 1. Experimental setup for SS-FSC extruded wire additive manufacturing via directed energy deposition with a laser beam and wire feedstock (DED-LB/w), (A) Illustration of the SS-FSC wire manufacturing, (B) The SS-FSC wire feeding system (Adopted from the feeder manual [20]), (C) House-developed DED-LB/w system.

firstly ground by silicon carbide grit papers and then polished by 1  $\mu m$ , 0.25  $\mu m$  alcohol-based diamond suspension. The finishing mechanical polishing was conducted by 40 nm colloidal silica suspension. After the mechanical grinding and polishing, samples were ion polished using Gatan PECS II model 685. Electron Back-Scattered Diffraction (EBSD) was operated on a JEOL JSM-7900F Scanning Electron Microscope (SEM) equipped with an Oxford Instrument Symmetry EBSD detector. The accelerating voltage for EBSD scanning was 20 kV. The step size of the EBSD scanning was set to 1  $\mu m$ . To reveal the microstructure evolution along the building direction (BD), 18 EBSD maps under a magnification of  $\times 100$  were captured and stitched into a large EBSD map. EBSD data were collected, processed and analysed by Aztec and AztecCrystal software. For microstructure investigation, the

longitudinal direction of the track (i.e. laser scanning direction) is denoted as LD. The transverse direction of the track is denoted as TD. The building direction of the track is denoted as BD.

#### 3. Results and discussion

#### 3.1. Track morphology and process mapping

To achieve sound deposition and demarcate the melting regimes as a function of the processing parameters, single-track experiments were conducted using the processing parameters (Table 2), across a wide range of specific energy densities ( $E_{\nu}$ ), from 93  $kJ \cdot s \cdot g^{-1} \cdot cm^{-2}$  to 304  $kJ \cdot s \cdot g^{-1} \cdot cm^{-2}$ . Note that the specific energy density  $E_{\nu}$  represents

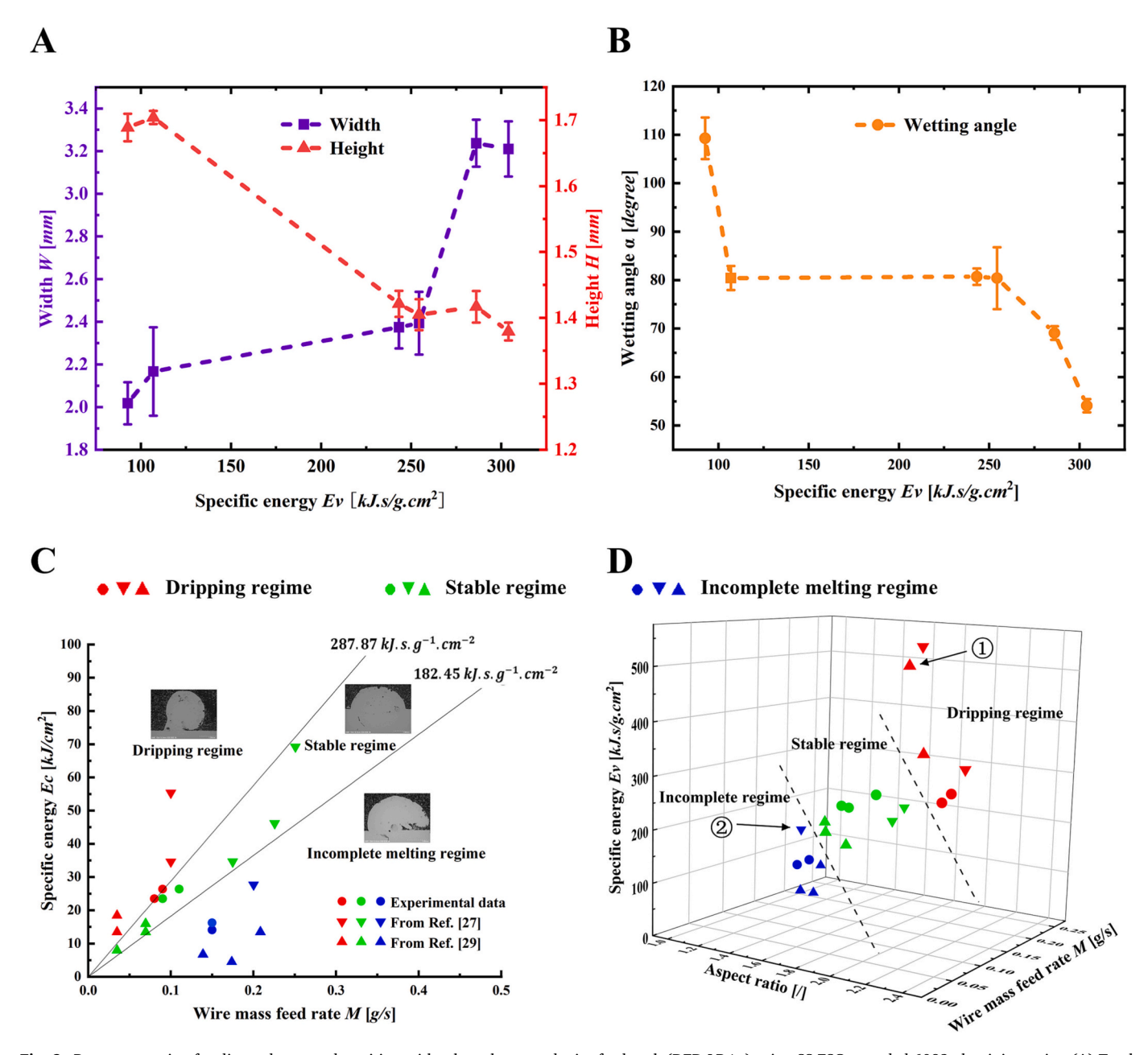


Fig. 2. Process mapping for directed energy deposition with a laser beam and wire feedstock (DED-LB/w) using SS-FSC extruded 6082 aluminium wire. (A) Track width and height, (B) Wetting angle, (C) 2D process mapping with wire mass feed rate and specific energy density  $E_c$ . Note that the specific energy density  $E_c = P / (v \cdot D)$  indicates the energy input per unit area by the laser, where P is the laser power, v is the scan speed, and D is the diameter of the laser spot. (D) 3D process mapping with aspect ratio, wire mass feed rate and specific energy density  $E_v$ . Note that the specific energy density  $E_v = P / (v \cdot M \cdot D)$  represents the amount of energy delivered per unit area for the per unit mass of material being processed, M is the wire mass feed rate. The datasets of DED-LB/w that are labelled as upward triangles and downward triangles are cited from Huang W et al. [21] (Fig. 7) and Zapata Avelino et al. [22] (Fig. 6), respectively.

the amount of energy delivered per unit area for the per unit mass of material being processed, which is defined as  $E_{\nu} = P/(\nu \cdot M \cdot D)$ , where P is the laser power,  $\nu$  is the laser scanning speed, D is the diameter of the laser spot, and M is the wire mass feed rate. It should be noted that all specific energy density values presented in this study were calculated using the laser power setting to provide a consistent basis for evaluation.

Fig. 2 shows the measured track widths, heights (Fig. 2 A) and wetting angles (Fig. 2 B) as well as the process mapping (Fig. 2 C and D) for the SS-FSC extruded 6082 aluminium wire deposition. As seen from Fig. 2 A, the track width increases with an increase of specific energy density  $E_{\nu}$ , while the track height decreases, which aligns with the previous experimental findings [21]. Those changes indicate that a higher  $E_{\nu}$  tends to induce a large melt droplet with increased wetting with the substrate, thereby increasing the track width while decreasing the track height. To verify this hypothesis, a quantitative analysis of the wetting angles at different specific energies was conducted, as shown in Fig. 2 B. As the laser energy density  $E_v$  increases, the wetting angle decreases, and once  $E_{\nu}$  exceeds a critical threshold of 254  $kJ \cdot s \cdot g^{-1} \cdot cm^{-2}$ , the wetting angle decreases sharply, revealing a nonlinear relationship between the energy density  $E_{\nu}$  and the wetting angle. This behaviour is mainly driven by surface tension at the three-phase contact point, which causes movement along the contact line. The current work reveals similarities between the process map of SS-FSC extruded wire and the general trends observed with commercial aluminium alloy wires regarding the influence of key process parameters (e.g., laser power, wire feed rate, traverse speed) on the geometric dimensions of deposited tracks [22,23]. Specifically, it was reported that an increase in laser power could bring about an increase in deposit width while a reduction in deposit height. This consistency suggests that, despite the unique origin of the raw feedstock material, its processing behaviour in the DED-LB/w process is mainly governed by similar fundamental physical and metallurgical principles of Al alloys.

As shown in Fig. 2 C, three process regimes can be observed during the manufacturing experiments using the SS-FSC extruded wire: (i) incomplete melting regime; (ii) stable regime; and (iii) dripping regime, characterised by the three types of transverse cross-sectioning morphologies. To better illustrate the different regimes, we use the specific energy density  $E_c$  to address the process. The specific energy density  $E_c$ indicates the energy input per unit area by the laser, which is defined as  $E_c = P/(\nu \cdot D)$ . Notably, the stable regime is located within an  $E_\nu$  range of  $183 \, kJ \cdot s \cdot g^{-1} \cdot cm^{-2}$  to  $288 \, kJ \cdot s \cdot g^{-1} \cdot cm^{-2}$ , and a semi-circular-shaped transverse cross-section profile can be obtained. Once the energy density  $E_{\nu}$  exceeds the critical threshold value of 288 kJ·s·g<sup>-1</sup>·cm<sup>-2</sup>, the melting regime changes to a dripping regime that is characterised by a large droplet profile under poor wetting with the substrate. This dripping regime is due to the excessive heat input that is being delivered to the wire, causing the wire to be melted and form droplets that drip from the metal wire before reaching the melt pool. Accordingly, instead of being smoothly transferred to the melt pool, those dripped droplets will lead to irregular and discontinuous depositions. Therefore, this dripping regime is undesirable and can severely impact track formation's precision and reliability [24]. By contrast, an incomplete melting regime occurs when the  $E_v$  input is below the value of 183  $kJ \cdot s \cdot g^{-1} \cdot cm^{-2}$ . This incomplete melting regime is attributed to insufficient energy input to the wire, resulting in partial melting of the wire and the formation of lack-of-fusion defects. Thus, this incomplete melting regime is also undesirable and can severely impact the stability of the track deposition T251.

Fig. 2 D presents the relationships between the melt pool aspect ratio, wire mass feed rate and specific energy  $E_{\nu}$ , highlighting the effect of  $E_{\nu}$  on the aspect ratio of the track, and then, in turn, affects the quality of the deposition layer. As shown at Point 1 in Fig. 2 D, the aspect ratio reaches 2.26 at a high specific energy density  $E_{\nu} = 531 \ kJ \cdot s \cdot g^{-1} \cdot cm^{-2}$  that leads to the dripping regime. By contrast, at a lower  $E_{\nu}$  with value of  $138 \ kJ \cdot s \cdot g^{-1} \cdot cm^{-2}$ , marked by Point 2 where the aspect ratio is decreased

to 1.01, resulting in the incomplete melting regime. Therefore, it is hypothesised that the aspect ratio serves as a crucial indicator for the deposition regimes, where the variations in specific energy density  $E_{\nu}$  can directly affect the track's integrity and stability. As observed, the wire mass feed rate (M) also has a significant impact on the track quality. As the wire mass feed rate increases, the melting regime transitions into an incomplete melting regime. Conversely, when the wire mass feed rate decreases, the melting regime shifts into a dripping regime. When the wire mass feed rate is around 0.11 g·s<sup>-1</sup>, the track reaches a stable deposition state, with droplets depositing uniformly and the melt pool stabilising.

In order to provide a comprehensive context for the process mapping, selected data points from previous studies [21,22] were incorporated into the process map. These studies employed similar DED-LB/w setups and Al alloy wire compositions. Comparative analysis reveals that most literature data align well with the trends observed in this work, particularly in the low-to-medium power range. Slight deviations in track geometry can be attributed to differences in laser spot size, shielding gas conditions, or wire manufacturing methods. This agreement across studies reinforces the reliability of the identified parameter–geometry correlations.

In this study, the Al alloy wire prepared by SS-FSC exhibits highly similar processing characteristics in DED-LB/w compared to those of conventional commercial wires. Notably, its stable deposition regime, melt pool dynamics, and response to energy density closely align with the behaviours reported for those of commercialised Al alloy feedstocks [22]. This similarity suggests that, despite originating from industrial by-products, the SS-FSC extruded wire demonstrates consistent processing performance during the DED-LB/w process. Accordingly, these findings provide compelling evidence that SS-FSC extruded wire may not only be a technically viable alternative to conventional feedstock but also a promising and sustainable solution for advanced metal additive manufacturing.

#### 3.2. Microstructure characterisation and analysis

Fig. 3 presents the microstructure of the built sample in its transverse cross-section at the middle of the track length. As shown in Fig. 3 A, a semi-circular shaped build profile with an aspect ratio of 1.67, built in a stable regime at  $E_v = 243 \, kJ \cdot s \cdot g^{-1} \cdot cm^{-2}$ . Randomly distributed pores with spherical shapes can also be observed. These are assumed to be gas pores and will be discussed in Section 3.3. Fig. 3C shows the microstructure of the SS-FSC extruded 6082 aluminium DED-LB/w track cross-section along the track height centreline, revealing grain size changes from the bottom to the top region. At the bottom of the track, relatively large columnar grains (average grain width  $18.8 \pm 3.2 \, \mu m$ along the transverse direction (TD)) are observed. This is due to the low solidification rate (*R*) in the bottom of the melt pool, where the normal to the local solidification front is nearly perpendicular to the laser scanning direction ( $\theta \approx 90^{\circ}$ ) [26], resulting in a relatively high G/Rvalue (Fig. 3 B-iii), which promotes the formation of columnar grains as shown in the solidification map Fig. 3 C-i. As illustrated in Fig. 3 B-ii, in the middle of the track, the equilibrium between thermal gradient and solidification rate creates favourable conditions for cellular grain development, and the grains exhibit a cellular structure. The grains with an average width of  $13.3 \pm 2.8 \,\mu m$  along TD are observed (Fig. 3 C-ii). The top of the track also consists primarily of cellular grains with an average size of  $8.9 \pm 1.8 \,\mu m$  (Fig. 3 C-iii).

The EBSD analysis (Fig. 4) provides the microstructure evolution within the melt pool region and its adjacent areas during DED-LB/w. Fig. 4 A illustrates the cross-sectional EBSD map of the track, with magnified views of different regions marked by coloured squares. The grain structures and orientations exhibit distinct spatial variations that reflect localised thermal gradients, solidification rates, and solidification mechanisms [27]. The bottom region of the melt pool shows an average

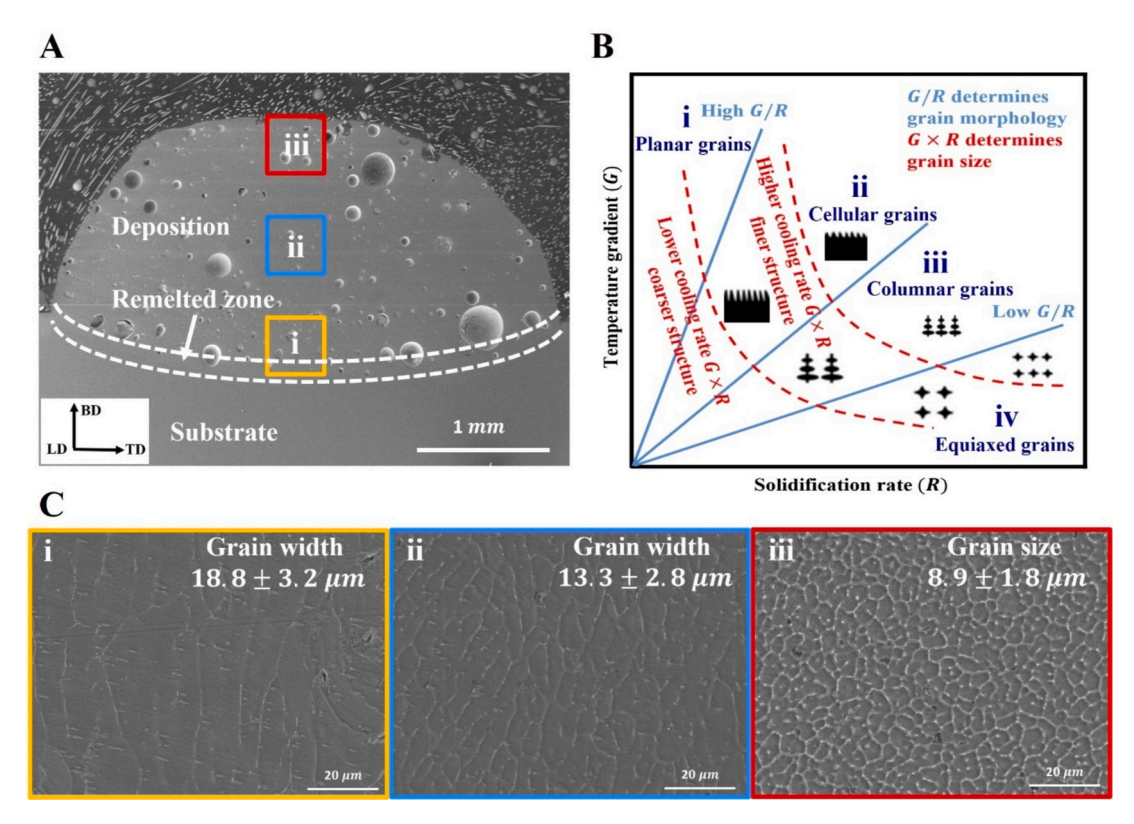


Fig. 3. Microstructure characterisation of the transverse cross-section of laser-wire directed energy deposition track using SS-FSC extruded 6082 aluminium wire. (A) SEM of the transverse cross-section of the track with laser power 3.8 kW, scanning speed 0.8 cm·s<sup>-1</sup> and wire feed rate 2.0 cm·s<sup>-1</sup>. The three different height locations in the final track were marked with red, blue and yellow squares, respectively, corresponding to the top, middle, and bottom zones of the transverse cross-section. (B) Schematic diagram of thermal gradient (*G*) and solidification rate (*R*) map for microstructure evolution (Adopted from reference [26]). (C) Magnified views of the microstructure at different heights within the track transverse cross-section, corresponding to the bottom (i), middle (ii), and top region (iii) shown in (A). The grain width and grain size were measured along the transverse direction (TD). (For interpretation of the references to colour in this figure legend, the reader is referred to the web version of this article.)

grain size of 34.5  $\mu m$ . Well-defined columnar grains at the interface are inclined toward the pool centre, which is associated with the direction of the thermal gradient. These grains display strong crystallographic directionality, with their < 100 > direction aligned along the direction from the deposited layer to the base material (i.e. negative direction of BD), indicating directional solidification. This phenomenon is driven by a high thermal gradient and a relatively slow solidification rate, which facilitates columnar grain growth [28,29]. The transition from the substrate to the deposited track reveals a sharp discontinuity in grain orientation and morphology, underscoring the significant thermal and microstructural changes induced by the DED-LB/w process. In the middle of the track, the grains exhibit the characteristics of cellular grains with subgrains and cell structures. The average grain size can be determined as 45.4  $\mu m$ . In contrast, the texture intensity becomes weaker in this region and the < 100 > is no longer aligned along BD. The thermal conditions in this region with moderate solidification rates and thermal gradients can promote the preferential growth of cellular grains originating from the bottom layer. The top region of the track is also dominated by cellular grains with subgrain structures. The average grain size can be determined as 46.3  $\mu$ m. The texture intensity is also weaker than the bottom region. The microstructure and texture in the top layer and middle layer are quite similar but significantly different from the bottom layer. It can be found that the average grain size of the middle and top layers extracted from the EBSD maps and OM images are different. This is because the OM images are based on the etching results, reflecting all the boundary information, including high-angle grain boundaries (HAGBs) and low-angle grain boundaries (LAGBs). While the grain size extracted from EBSD maps was based on the crystallographic direction, taking the regions enclosed by HAGBs as grains. It should be

noted small subgrains could be identified in the marked regions of ii and iii as shown in Fig. 4C. Overall, the microstructural evolution across the melt pool reflects the thermal dynamics of the DED-LB/w process.

In terms of microstructural characteristics, it can be found that the morphology of the deposited track exhibits no difference compared to DED-LB/w deposits produced with commercial wires. Specifically, whether using SS-FSC extruded wire or conventional commercial wire, the solidifying melt pool predominantly exhibits a typical columnar or equiaxed grain structure [13,14]. This phenomenon suggests that despite the unique by-product origin and absence of conventional post-processing of the SS-FSC extruded wire, its solidification mechanism within the laser-induced melt pool is also governed by the fundamental physical principles [27]. This similarity implies the SS-FSC extruded wire is feasible for DED-LB/w additive manufacturing.

## 3.3. Porosity defect analysis

Porosity formation in DED-LB/w additive manufacturing is governed by complex multi-physics, mainly including laser-vapour-melt interactions on keyhole collapse pores, gas-liquid interactions with gas entrapment pores, and the competing influences of gravity, drag, thermocapillary and buoyancy forces on bubble growth and subsequent trapping within the melt pool. These pores primarily originate from two sources [30,31]: (I) improper processing conditions and (II) feedstock (e. g., wire, substrate, shielding gas and air) gas entrapment.

As shown in Fig. 5 A, most pores observed in the transverse cross-section exhibit a spherical morphology with equivalent diameters of approximately  $20-50 \, \mu m$ . We hypothesise that those pores are mostly gas pores, mainly arising from three feedstock sources (Fig. 6 A): (I)

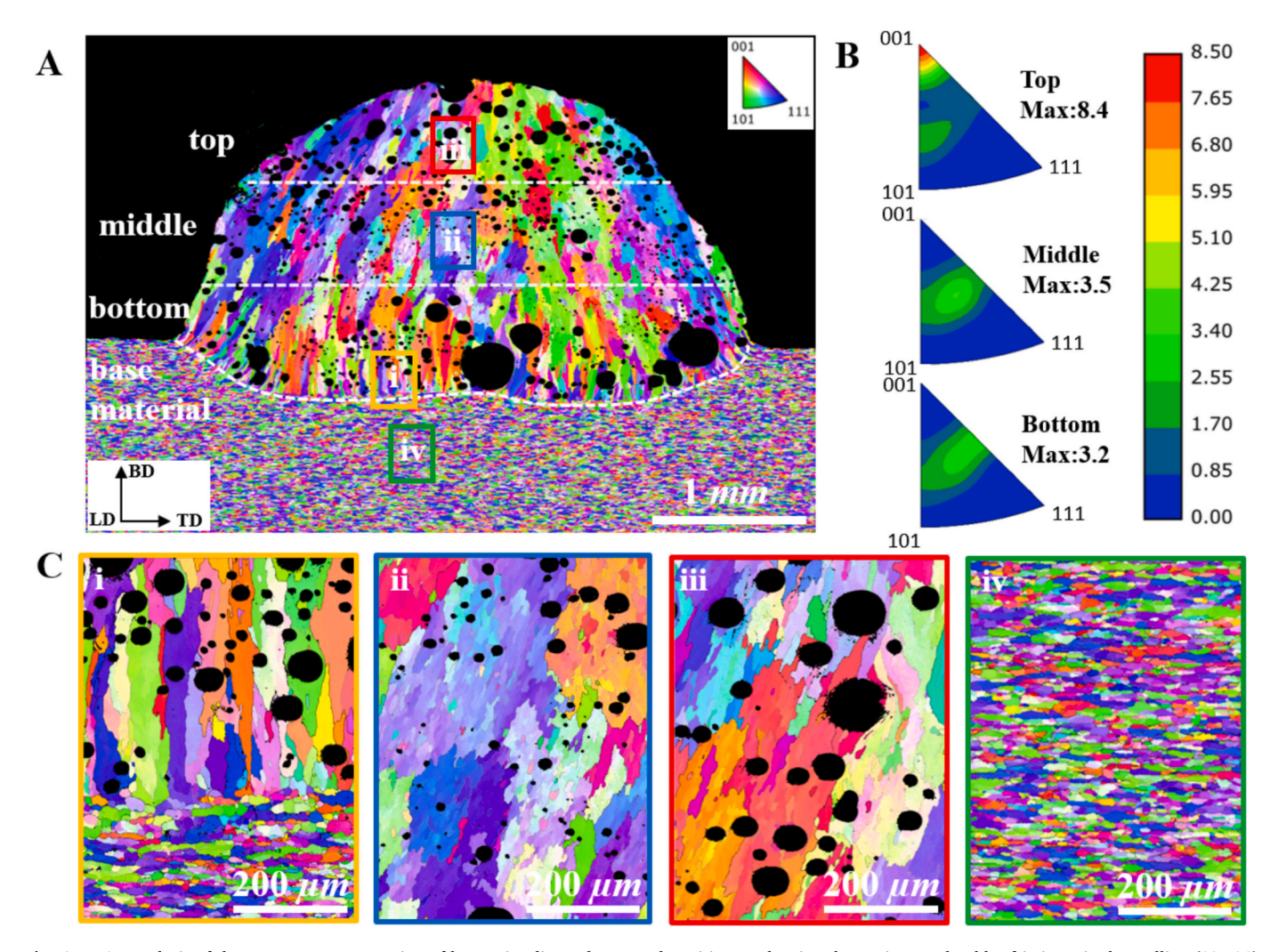


Fig. 4. EBSD analysis of the transverse cross-section of laser-wire directed energy deposition track using the stationary shoulder friction stir channelling (SS-FSC) extruded 6082 aluminium wire (laser power  $3.8 \, kW$ , scanning speed  $1.3 \, cm \cdot s^{-1}$ , and wire feed rate  $2.8 \, cm \cdot s^{-1}$ ). Inverse Pole Figure (IPF)-Z//LD. (A) EBSD of the transverse cross-section of the track. The four different height locations in the final track were marked with a red square, a deep blue square, a yellow square, and a green square, representing the corresponding top, middle, and bottom depths of the track and substrate. (B) The scale bar length in (C)-i, (C)-ii and (C)-iii. (C) magnified views at different heights, corresponding to the interface between the substrate and track (i), the track middle (ii), the track top (iii), and the substrate (iv). (For interpretation of the references to colour in this figure legend, the reader is referred to the web version of this article.)

oxide films and contaminations (e.g., residual moisture) of the SS-FSC extruded aluminium wire [24]; (II) substrate materials, including oxide layers on the surface of the substrate or pre-existing pores within the substrate, both of which can contribute to the formation of pores in the melt pool under thermal cycling conditions [30]; and (III) entrapment of shielding gas or air, where these gases could be entrapped in the melt pool during the deposition process, particularly when insufficient shielding gas or inadequate purity of shielding gas is provided [31]. These gas sources mentioned above, either individually or collectively, influence the formation and distribution of porosity within the track.

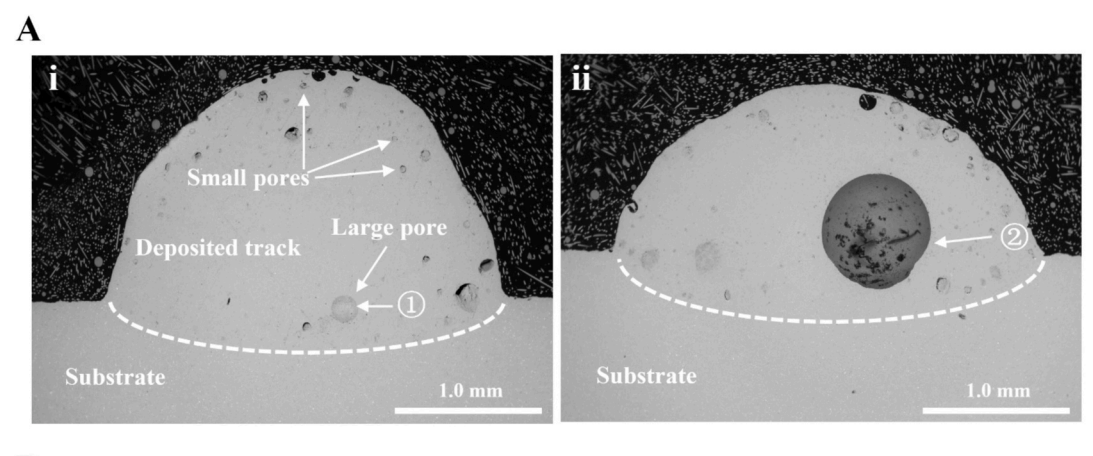
Based on the EDS analysis as shown in Fig. 5B, the regions surrounding pore No. 1, which are the content of aluminium oxide, exhibited an oxygen content of 11.8 wt% and a nitrogen content of 3.7 wt% (Fig. 5 B-iii). These findings are consistent with our hypothesis on the entrapment gas sources (source III above). The previous study [32] also reported that the high temperature of the melt pool in the DED-LB/w process for aluminium deposition can induce the decomposition of aluminium oxides. Consequently, oxygen could also be derived from the oxides of wire and substrate material in the DED-LB/w process, as stated in sources I and II above.

Large pores were also observed over the transverse cross-sections (Fig. 5 A), showing equivalent diameters of approximately 200-

500  $\mu$ m. We hypothesised that the formation of these large pores is attributed to the coalescence of small pores. This coalescence phenomenon is frequently observed in laser-based additive manufacturing processes and is generally driven by surface tension [33]. Small bubbles circulate and migrate within the melt pool due to Marangoni shear flow, increasing the bubble collision probability. As illustrated in Fig. 6 A, when the liquid film between colliding small bubbles ruptures, coalescence driven by surface tension occurs. This is because the coalescence minimises the total surface area of the bubbles, thereby reducing the whole system's surface-free energy [31]. Those small bubbles coalescence ultimately leads to the formation of large bubbles. Note that those large bubbles may remain relatively stable in the melt pool for an extended period due to the high viscosity of the melted metal (Fig. 6 A).

For bubbles to successfully escape from the melt pool, they must avoid being captured by the melt pool solidification front, which depends on two key conditions. First, the upward buoyancy force acting on the bubbles must exceed the downward force induced by the Marangoni shear flow. Second, the bubble's rising rate must be greater than the solidification rate of the melt pool. Otherwise, as illustrated in Fig. 6 B, bubbles can be entrapped by the solidification front, resulting in porosity defects.

As previously discussed, the feedstock plays a crucial role in porosity



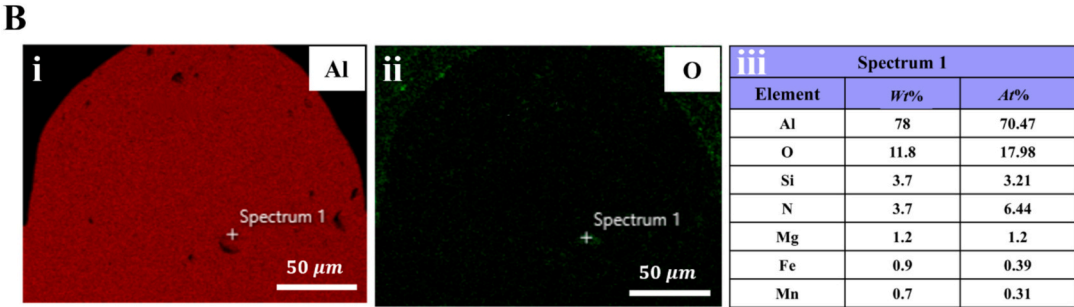


**Fig. 5.** (A) Pore morphology in transverse cross-section of laser-wire directed energy deposition track using the stationary shoulder friction stir channelling (SS-FSC) extruded 6082 aluminium wire. (A)-i The deposited track was produced with a laser power of  $3.8 \, kW$ , a scanning speed of  $0.8 \, cm \cdot s^{-1}$ , and a wire feed rate of  $2.0 \, cm \cdot s^{-1}$ . This condition falls within the stable regime. (A)-ii The deposited track was produced with a laser power of  $3.8 \, kW$ , a scanning speed of  $0.8 \, cm \cdot s^{-1}$ , and a wire feed rate of  $1.5 \, cm \cdot s^{-1}$ . This condition falls within the dripping regime. (B) EDS mapping of aluminium element (i), oxygen element (ii), and comparative mass and atomic percentages of aluminium, oxygen, and nitrogen elements (iii) in the regions surrounding the pore No. 1.

formation during the DED-LB/w process. To further investigate this influence, a detailed characterisation of the SS-FSC Al wire was conducted using SEM. As shown in Fig. 6 C, the compositional heterogeneity can be detected in the cross-section of the SS-FSC wire. Point EDS analysis conducted at the locations (Point 1 in Fig. 6 C-ii) demonstrates a relatively high oxygen content (25.62 %), alongside aluminium (72.72 wt%) and other trace elements (Si: 0.84 wt%, Mg: 0.29 wt%, Mn: 0.4 wt%, Fe: 0.13 wt%). This provides direct evidence for the presence of oxide films and potential contamination on the wire surface, which may have originated from the SS-FSC extrusion process or subsequent environmental exposure. These findings support the hypothesis that the surface condition of the SS-FSC wire, such as oxide films and contaminants, plays a significant role in the formation of gas porosity during the DED-LB/w process.

To further reveal the mechanisms of bubble escape and entrapment, the bubble escape rate during the DED-LB/w process was calculated. The rate of bubble escape can be estimated using the following formula derived from Stokes' law [34]:  $V_f = 2(\rho_l - \rho_g) \cdot gr^2 \cdot (9\mu_l)^{-1}$ , where  $V_f$  is the rate of bubble escape,  $\rho_l$  is the density of the liquid metal,  $\rho_\sigma$  is the density of the gas, g refers to the gravitational acceleration, r is the radius of the pore, and  $\mu_l$  refers the viscosity of the liquid metal. According to Stokes' law, the rate of bubble escape is directly proportional to its radius and inversely proportional to the viscosity of the liquid metal. In this study, based on the parameter values shown in Appendix. Table 1, the escape rate of Pore No. 1 (Fig. 5 A-i) was calculated to be  $0.23 \text{ cm} \cdot \text{s}^{-1}$ . If the solidification rate of the melt pool exceeds the escape rate of the pore, the pore will be captured by the solidification front. Previous studies [26] have shown that in laser directed energy deposition, the maximum solidification rate of the melt pool can be approximated by the laser scanning speed. In this process, the laser scanning speed is  $0.8 \text{ cm} \cdot \text{s}^{-1}$ , which is much higher than the escape rate of the

pore No.1. As a result, the pore is captured by the solidification front, leading to the formation of a pore. When the process conditions are optimised to achieve an escape rate above the critical threshold, the formation of pores will be significantly reduced.

In addition to the feedstock porosity [31], improper processing parameters also play a crucial role in the porosity formation [35]. For instance, at the same energy density ( $E_c = 26.39 \text{ kJ} \cdot \text{cm}^{-2}$ ), the excessive wire feed rate leads to a decrease in thermal input, which in turn causes an increase in cooling rate. As defined by the solidification kinetics relationship  $\dot{T} = G \cdot R$  [36], where  $\dot{T}$  is the cooling rate, R is the solidification rate, and G is the thermal gradient, an increase in cooling rate directly leads to a rise in solidification rate under a similar thermal gradient. This decreases melt pool lifetime and gas escape time, ultimately increasing the probability of pore formation. As observed in Fig. 5 A-i, at a higher wire feed rate of 2.0  $cm \cdot s^{-1}$ , numerous small pores formed in the deposited track. In contrast, at a lower wire feed rate of  $1.5 \text{ cm} \cdot \text{s}^{-1}$ , the number of pores at the top of the track was severely reduced (Fig. 5 A-ii). In addition, as shown in Fig. 5 A-ii, a large pore No. 2 (equivalent diameter of 400  $\mu$ m) can be detected in the cross-section. This phenomenon is primarily attributed to the fact that a lower wire feed rate increases effective heat input. The increased heat input prolongs the lifetime of the melt pool, facilitating the coalescence and growth of small bubbles within the melt. In conclusion, this leads to the formation of large bubbles. It demonstrates that the wire feed rate plays a crucial role in affecting pore size and quantity.

## 3.4. Microhardness of the single track

Fig. 7 shows the microhardness distribution across the transverse cross-section of the DED-LB/w deposited track using SS-FSC extruded 6082 Al wire. The microhardness in the substrate region remains relatively high (95–100  $HV_{0.5}$ ), which is consistent with the T6-treated state

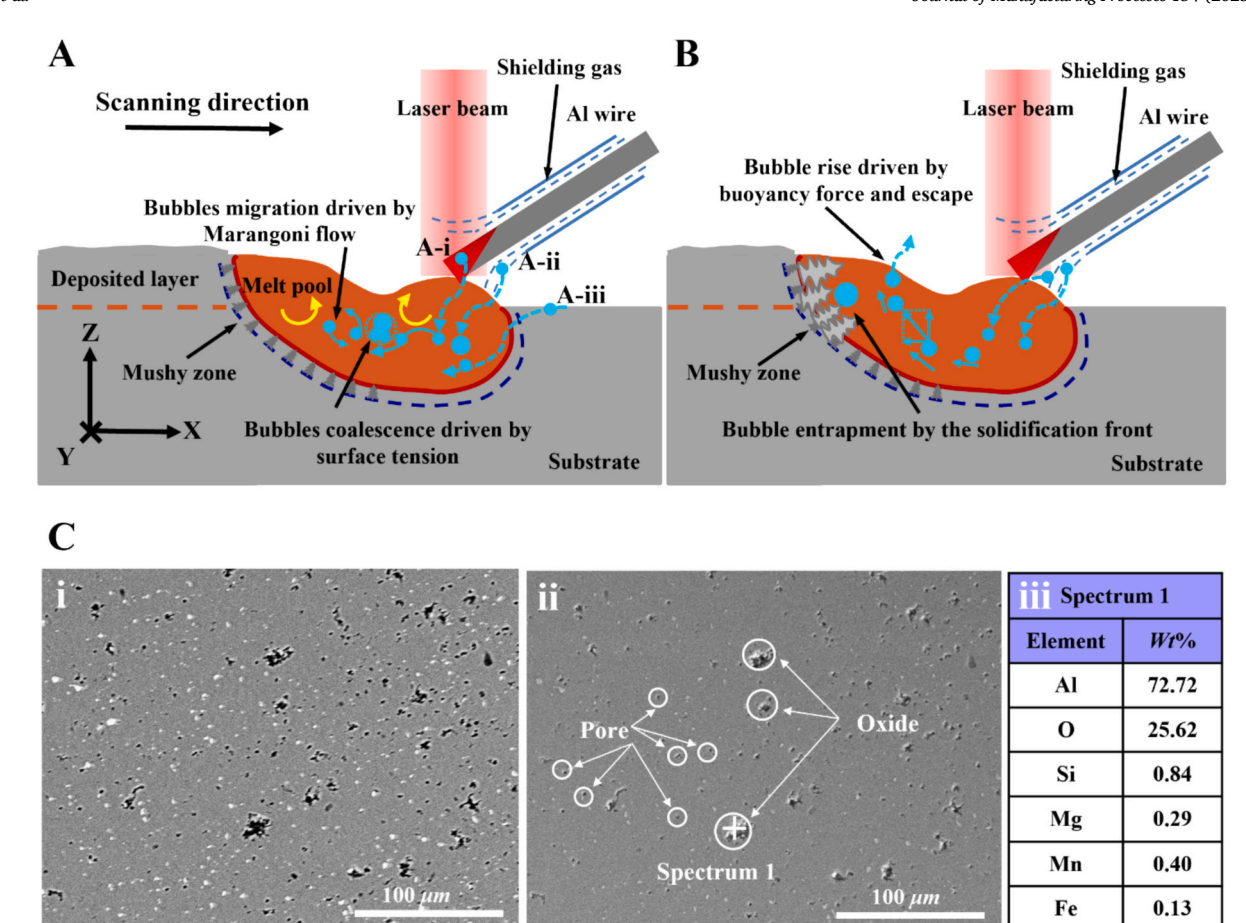
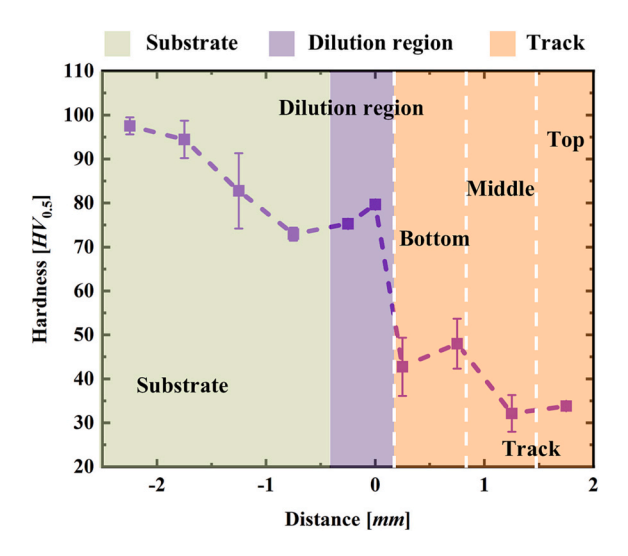


Fig. 6. (A) Schematic diagram illustrating the migration and coalescence of small bubbles in the melt pool, driven by Marangoni flows and surface tension. A-i represents bubbles originating from the SS-FSC extruded aluminium wire, A-ii represents bubbles caused by shielding gas or air, and A-iii represents bubbles originating from the substrate. (B) Schematic diagram of bubble entrapment by the solidification front and escape from melt pool driven by the buoyancy force. (C) SEM observation of the transverse cross-section of the SS-FSC extruded Al wire. (C)-i Backscattered Electrons (BSE) analysis of the wire. (C)-ii SEM observation of the same cross-section. (C)-iii Comparative mass percentages of aluminium, oxygen, and other trace elements at point 1.



**Fig. 7.** The measured microhardness along the centreline of the DED-LB/w deposited track in the transverse cross-section. Scanning speed of 1.3  $cm \cdot s^{-1}$ , a laser power of 3.8 kW, a wire feed rate of 2.8  $cm \cdot s^{-1}$ , and an energy density (Ev) of 107  $kJ \cdot s \cdot g^{-1} \cdot cm^{-2}$ . The reference point (0 mm) corresponds to the interface between the deposited track and the substrate surface.

of the base material. In contrast, a gradual reduction in microhardness can be observed toward the deposited direction, with values decreasing to approximately 30–50  $HV_{0.5}$  in the upper track. This softening behaviour is attributed to the thermal cycles associated with laser deposition and the intrinsic metallurgical condition of the feedstock. According to a previous study [13], the as-received SS-FSC extruded 6082 Al wire exhibited a lower microhardness (53.36  $HV_{0.5}$ ), compared to the original 6082-T6 sheet (113  $HV_{0.5}$ ), due to the dissolution of precipitation-strengthening phases during the SS-FSC process. In this study, the microhardness values measured in the track are slightly lower than those of the SS-FSC wire. This could be attributed to the lack of reprecipitation, coarser grains, and internal porosity. To address this issue, further post-process thermal treatments for the SS-FSC produced wire are expected to restore precipitation hardening and enhance mechanical properties.

The SS-FSC extruded wire as a feedstock for DED-LB/w differs from conventional commercial wires. The wire's origin as a by-product during subsurface channel fabrication directly contributes to enhanced resource efficiency and significant sustainability advantages. However, its use without the typical post-processing steps (e.g., surface oxide film removal) applied to commercial wires leads to porosity during the DED-LB/w process, primarily attributed to unremoved oxide films and potentially entrapped gases. Nevertheless, the process map for this wire shows no significant differences from that of conventional commercial Al wire in additive manufacturing. Furthermore, the microstructure morphology of the track is similar to that produced with commercial wires (e.g., typical columnar or equiaxed grains), indicating analogous

solidification mechanisms within the melt pool despite the unique raw material source. It is precisely this ability to valorise an industrial byproduct that constitutes the unique value and immense potential of SS-FSC extruded wire as an alternative, sustainable feedstock.

#### 4. Conclusions

The study investigates the processing of the stationary shoulder friction stir channelling (SS-FSC) extruded aluminium wire, 'by-products' produced by Severe plastic deformation (SPD), using directed energy deposition with a laser beam and wire feedstock (DED-LB/w) additive manufacturing. Process mapping was established to demarcate the manufacturing regimes of stable, dripping, and incomplete melting, across an extensive energy density (92 to  $303\,kJ\cdot s\cdot g^{-1}\cdot cm^{-2}$ ). Metallurgy tests were conducted to reveal the microstructure evolution and the formation of porosity defects across the deposited tracks. The porosity source was primarily attributed to improper processing conditions and feedstock. It can be found that the SS-FSC extruded aluminium wire exhibits significant potential for application in additive manufacturing. Notably, the recycling utilisation of the SS-FSC generates 'by-products' that reduce material waste and support the advancement of a circular economy.

The key findings are summarised as follows:

- (1) DED-LB/w processing was conducted with a novel SS-FSC extruded aluminium wire feedstock, showing that stable depositions can be achieved. Thus, the SS-FSC extruded wire exhibits high potential for DED-LB/w additive manufacturing.
- (2) DED-LB/w process mapping for the SS-FSC extruded aluminium wire revealed three distinct processing regimes: stable, dripping, and incomplete melting. The transition between incomplete melting and stable regime occurred at a minimum laser energy density of 183 kJ·s·g<sup>-1</sup>·cm<sup>-2</sup>, while the transition to the dripping regime was observed at a maximum energy density of 288 kJ·s·g<sup>-1</sup>·cm<sup>-2</sup>.
- (3) The substructure morphology of the deposited track was transited from columnar to cellular grains along the built direction. The bottom of the track exhibited strong crystallographic directionality, with the <100> direction oriented from the deposited layer to the substrate and features columnar grains. In the middle of the track, the grains exhibited cellular characteristics with subgrains, where the texture intensity was relatively weak. The top of the track also exhibited cellular grains with subgrains.
- (4) Gas pores were observed in the transverse cross-section of the track. Porosity was primarily attributed to two sources: (I) improper processing parameters and (II) feedstock (e.g., wire, substrate, shielding gas and air) gas entrapment. Improper processing parameters, such as an excessive wire feed rate, can

increase the cooling rate, which in turn accelerates the solidification rate. This can result in pore formation due to bubble entrapment. Additionally, the oxide film and moisture from the feedstock or environment were responsible for the formation of gas pores. Large pores were generated by the coalescence of small ones, which was driven by surface tension.

This study demonstrates the feasibility of using aluminium wire, extruded via the SS-FSC process, as feedstock for the DED-LB/w additive manufacturing. The single-track deposition confirmed the suitability of wire for stable continuous deposition, strong metallurgical bonding, and dimensional stability, demonstrating its compatibility with conventional DED systems. Notably, the proposed approach aligns with the principles of circular economy and industrial symbiosis by converting manufacturing by-products into high-value functional components. These findings offer a viable pathway toward greener and more resource-conscious metal additive manufacturing practices.

#### CRediT authorship contribution statement

Yajie Chu: Data curation, Formal analysis, Methodology, Validation, Visualization, Writing – original draft. Xingjian Zhao: Formal analysis, Investigation, Writing – review & editing. Wanting Sun: Formal analysis, Writing – review & editing. Sam Holdsworth: Resources, Supervision, Writing – review & editing. Dikai Guan: Formal analysis, Investigation, Writing – review & editing. Yuze Huang: Conceptualization, Formal analysis, Investigation, Methodology, Project administration, Supervision, Writing – original draft, Writing – review & editing.

#### Declaration of competing interest

The authors declare that they have no known competing financial interests or personal relationships that could have appeared to influence the work reported in this paper.

#### Acknowledgements

This research is supported by the Royal Society International Exchanges (IEC\NSFC\233607) and the Interdisciplinary Catalyst Funding Lancaster University for Yuze Huang, UKRI Future Leaders Fellowship (MR/T019123/2, UKRI 1051) for Dikai Guan. The authors thank the support with additive manufacturing experiment from Amirhossein Sadeghian, Ragavendran Meenakshisundaram and Noppawee Wadee. The authors also thank the support with scanning electron microscopy (SEM) and energy dispersive X-ray spectroscopy (EDS) from Siyu Xu. The authors wish to acknowledge the support with stationary shoulder friction stir channelling (SS-FSC) trials conducted at TWI Ltd. provided by Nathan Horrex and Oliver Watts.

## Appendix A

Appendix. Table 1
Input parameters of Stokes' law [34].

Parameters [37]	No.1
Density of melt aluminium $\rho_l$ [g·cm <sup>-3</sup> ]	2.7
Density of oxygen $\rho_g$ [g·cm <sup>-3</sup> ]	0.001429
Gravitational acceleration g [cm·s <sup>-2</sup> ]	980
The radius of the oxygen pore $r$ [ $cm$ ]	0.02
Viscosity $\mu_l$ [mPa·s]	1.1

**Table 2**Processing parameters of the DED-LB/w process.

Sample	Laser power, P [kW]	Scanning speed, $\nu$ [cm·s <sup>-1</sup> ]	Laser sport size, D [cm]	Energy density, Ec [kJ-cm <sup>-2</sup> ]	Energy density, $Ev [kJ \cdot s \cdot g^{-1} \cdot cm^{-2}]$
01	3.8	1.3	0.18	16	107
02	3.8	1.5	0.18	14	93
03	3.8	0.8	0.18	26	243
04	3.8	0.8	0.18	26	286
05	3.8	0.8	0.18	26	304

Table 3
Microhardness measurements along the centreline of the DED-LB/w deposited track in the transverse cross-section. Note that the distance reference point (0 mm) corresponds to the interface between the deposited track and the substrate surface. M1, M2 and M3 represent different measurement trials.

Distance (mm)	-2.25	-1.75	-1.25	-0.75	-0.25	0.25	0.75	1.25	1.75
M1 (HV <sub>0.5</sub> )	98.7	88.2	71.3	75.7	78.9	42.8	45.3	34.7	34.2
$M2 (HV_{0.5})$	94.4	87.2	73.4	76	79.9	36.1	54.5	27.3	34.2
M3 (HV <sub>0.5</sub> )	90.2	72.9	74.1	74.2	80.2	49.3	44.2	34.4	33

## Data availability

The data that support the findings of this study are available from the corresponding author upon reasonable request.

#### References

- [1] DebRoy T, Wei HL, Zuback JS, Mukherjee T, Elmer JW, Milewski JO, et al. Additive manufacturing of metallic components – process, structure and properties. Prog Mater Sci 2018;92:112–224. https://doi.org/10.1016/j.pmatsci.2017.10.001.
- [2] Svetlizky D, Das M, Zheng B, Vyatskikh AL, Bose S, Bandyopadhyay A, et al. Directed energy deposition (DED) additive manufacturing: physical characteristics, defects, challenges and applications. Mater Today 2021;49:271–95. https://doi. org/10.1016/j.mattod.2021.03.020.
- [3] Svetlizky D, Zheng B, Vyatskikh A, Das M, Bose S, Bandyopadhyay A, et al. Laser-based directed energy deposition (DED-LB) of advanced materials. Mater Sci Eng A 2022;840:142967. https://doi.org/10.1016/j.msea.2022.142967.
- [4] Sæterbø M, Solvang WD. Metal additive manufacturing adoption in SMEs: technical attributes, challenges, and opportunities. J Manuf Process 2024;128:175–89. https://doi.org/10.1016/j.jmapro.2024.07.074.
- [5] He W, Shi W, Li J, Xie H. In-situ monitoring and deformation characterization by optical techniques; part I: laser-aided direct metal deposition for additive manufacturing. Opt Lasers Eng 2019;122:74–88. https://doi.org/10.1016/j. optlaseng. 2019.05.020.
- [6] Kanishka K, Acherjee B. A systematic review of additive manufacturing-based remanufacturing techniques for component repair and restoration. J Manuf Process 2023;89:220–83. https://doi.org/10.1016/j.jmapro.2023.01.034.
- [7] Hagenlocher C, O'Toole P, Xu W, Brandt M, Easton M, Molotnikov A. In process monitoring of the thermal profile during solidification in laser directed energy deposition of aluminium. Addit Manuf Lett 2022;3:100084. https://doi.org/ 10.1016/j.addlet.2022.100084.
- [8] Ai Y, Wang Y, Han S, Ye C. Investigation of cladding layer formation in uphill wire laser additive manufacturing on inclined substrate. Appl Therm Eng 2024;247: 122919. https://doi.org/10.1016/j.applthermaleng.2024.122919.
- [9] Pietro VD, Gandra J, Clarke A, Hockaday J, Law R. Removing design and manufacturing complexity from integrated thermal management solutions using friction stir channelling. In: 2022 38th semiconductor thermal measurement, modeling & management symposium (SEMI-THERM), San Jose, CA, USA; 2022.
- [10] Duflou JR, Wegener K, Tekkaya AE, Hauschild M, Bleicher F, Yan J, et al. Efficiently preserving material resources in manufacturing: industrial symbiosis revisited. CIRP Ann 2024;73:695–721. https://doi.org/10.1016/j. cirp.2024.05.006
- [11] Schwab S, Selin R, Voron M. Welding materials for TIG welding, surfacing, and WAAM technology of titanium alloys. Weld World 2023;67:981–6. https://doi. org/10.1007/s40194-023-01464-z.
- [12] Buffa G, Campanella D, Adnan M, La Commare U, Ingarao G, Fratini L. Improving the industrial efficiency of recycling aluminum alloy chips using friction stir extrusion: thin wires production process. Int J Precis Eng Manuf Green Technol 2024;11:1133–46. https://doi.org/10.1007/s40684-023-00573-w.
- [13] Yuan L, Zeng X, Zhao X, Xie Y, Gandra J, Guan D. Microstructure evolution and tensile behaviour of fine-grained 6082 Al wire with high ultimate strength and high work hardening by friction stir extrusion of bulk Al sheet. Mater Sci Eng A 2023;864:144589. https://doi.org/10.1016/j.msea.2023.144589.

- [14] Yuan L, Zeng X, Zhao X, Xie Y, Gandra J, Guan D. Dependence of microstructure evolution of novel CoreFlow™ aluminium alloy wire on wire diameter. J Mater Res Technol 2024;28:2442–54. https://doi.org/10.1016/j.jmrt.2023.12.177.
- [15] Zhao X, Zeng X, Yuan L, Gandra J, Hayat Q, Bai M, et al. A novel approach for producing Mg-3Al-1Zn-0.2Mn alloy wire with a promising combination of strength and ductility using CoreFlowTM. Scr Mater 2023;227:115301. https://doi.org/ 10.1016/j.scriptamat.2023.115301.
- [16] Ghanadi N, Pasebani S. A review on wire-laser directed energy deposition: parameter control, process stability, and future research paths. JMMP 2024;8:84. https://doi.org/10.3390/jmmp8020084.
- [17] Thompson SM, Bian L, Shamsaei N, Yadollahi A. An overview of direct laser deposition for additive manufacturing; part I: transport phenomena, modeling and diagnostics. Addit Manuf 2015;8:36–62. https://doi.org/10.1016/j. addma.2015.07.001.
- [18] Shamsaei N, Yadollahi A, Bian L, Thompson SM. An overview of direct laser deposition for additive manufacturing; part II: mechanical behavior, process parameter optimization and control. Addit Manuf 2015;8:12–35. https://doi.org/ 10.1016/j.addma.2015.07.002.
- [19] Gandra J. Method and apparatus for creating channels in workpieces. US 11,020,817 B2. 2021.
- [20] BINZEL wire feeding system (MFS-V3) manual. n.d. https://abidoc.binzel-bicor. com/uploads/ABIDOC/ROBOTIC\_SYSTEMS/Drahtfoer dersysteme/MFS\_V3\_ 1/Prospekte/PRO\_R158\_MFS-V3\_Bestellunterlage\_EN\_WEB.pdf.
- [21] Huang W, Chen S, Xiao J, Jiang X, Jia Y. Laser wire-feed metal additive manufacturing of the Al alloy. Opt Laser Technol 2021;134:106627. https://doi. org/10.1016/j.optlastec.2020.106627.
- [22] Zapata A, Bernauer C, Stadter C, Kolb CG, Zaeh MF. Investigation on the cause-effect relationships between the process parameters and the resulting geometric properties for wire-based coaxial laser metal deposition. Metals 2022;12:455. https://doi.org/10.3390/met12030455.
- [23] Huang Y, Khamesee MB, Toyserkani E. A new physics-based model for laser directed energy deposition (powder-fed additive manufacturing): from single-track to multi-track and multi-layer. Opt Laser Technol 2019;109:584–99. https://doi. org/10.1016/j.optlastec.2018.08.015.
- [24] Yi H, Yang L, Jia L, Huang Y, Cao H. Porosity in wire-arc directed energy deposition of aluminum alloys: formation mechanisms, influencing factors and inhibition strategies. Addit Manuf 2024;84:104108. https://doi.org/10.1016/j. addma.2024.104108.
- [25] Assad A, Bevans BD, Potter W, Rao P, Cormier D, Deschamps F, et al. Process mapping and anomaly detection in laser wire directed energy deposition additive manufacturing using in-situ imaging and process-aware machine learning. Mater Des. 2024;245:113281. https://doi.org/10.1016/j.matdes.2024.113281.
- [26] Huang Y, Ansari M, Asgari H, Farshidianfar MH, Sarker D, Khamesee MB, et al. Rapid prediction of real-time thermal characteristics, solidification parameters and microstructure in laser directed energy deposition (powder-fed additive manufacturing). J Mater Process Technol 2019;274:116286. https://doi.org/ 10.1016/i.jmatprotec.2019.116286.
- [27] Abuabiah M, Mbodj NG, Shaqour B, Herzallah L, Juaidi A, Abdallah R, et al. Advancements in laser wire-feed metal additive manufacturing: a brief review. Materials 2023;16:2030. https://doi.org/10.3390/ma16052030.
- [28] Liu X, Di Y, Wang G, Yuan Q, Rong Y. The thermal-flow dynamics of hydrogen bubbles in coaxial laser wire directed energy deposition of Al-Mg-Sc alloy. Addit Manuf 2025;98:104649. https://doi.org/10.1016/j.addma.2025.104649.
   [29] Huang W, Chen S, Xiao J, Jiang X, Jia Y. Investigation of filler wire melting and
- [29] Huang W, Chen S, Xiao J, Jiang X, Jia Y. Investigation of filler wire melting and transfer behaviors in laser welding with filler wire. Opt Laser Technol 2021;134: 106589. https://doi.org/10.1016/j.optlastec.2020.106589.

- [30] Wolff SJ, Wang H, Gould B, Parab N, Wu Z, Zhao C, et al. In situ X-ray imaging of pore formation mechanisms and dynamics in laser powder-blown directed energy deposition additive manufacturing. Int J Mach Tool Manuf 2021;166:103743. https://doi.org/10.1016/j.ijmachtools.2021.103743.
- [31] Zhang K, Chen Y, Marussi S, Fan X, Fitzpatrick M, Bhagavath S, et al. Pore evolution mechanisms during directed energy deposition additive manufacturing. Nat Commun 2024;15:1715. https://doi.org/10.1038/s41467-024-45913-9.
- [32] Ghosh PS, Sen A, Chattopadhyaya S, Sharma S, Singh J, Dwivedi SP, et al. Prediction of transient temperature distributions for laser welding of dissimilar metals. Appl Sci 2021;11:5829. https://doi.org/10.3390/app11135829.
- [33] Huang Y, Fleming TG, Clark SJ, Marussi S, Fezzaa K, Thiyagalingam J, et al. Keyhole fluctuation and pore formation mechanisms during laser powder bed fusion additive manufacturing. Nat Commun 2022;13:1170. https://doi.org/ 10.1038/s41467-022-28694-x.
- [34] Shearer SA, Hudson JR. Fluid mechanics: Stokes' law and viscosity n.d.
- [35] Vyskoč M. Effect of filler wire feed rate on the formation of porosity in laser welded joints of magnesium alloy AZ31B–H24. Metals 2023;13:460. https://doi.org/ 10.3390/met13030460.
- [36] M E G. Principles of solidification. Springer Science & Business Media; 2010.
- [37] ASM International. ASM handbook, volume 2: properties and selection: nonferrous alloys and special-purpose materials. ASM International; 1990.